

# Underpotential Deposition of 3D Transition Metals: Versatile Electrosynthesis of Single-Atom Catalysts on Oxidized Carbon Supports

A. Meese, D. Leshchev

To be published in "Advanced Materials"

February 2024

Photon Sciences

**Brookhaven National Laboratory**

**U.S. Department of Energy**

USDOE Office of Science (SC), Basic Energy Sciences (BES). Scientific User Facilities (SUF)

Notice: This manuscript has been authored by employees of Brookhaven Science Associates, LLC under Contract No. DE-SC0012704 with the U.S. Department of Energy. The publisher by accepting the manuscript for publication acknowledges that the United States Government retains a non-exclusive, paid-up, irrevocable, world-wide license to publish or reproduce the published form of this manuscript, or allow others to do so, for United States Government purposes.

## **DISCLAIMER**

This report was prepared as an account of work sponsored by an agency of the United States Government. Neither the United States Government nor any agency thereof, nor any of their employees, nor any of their contractors, subcontractors, or their employees, makes any warranty, express or implied, or assumes any legal liability or responsibility for the accuracy, completeness, or any third party's use or the results of such use of any information, apparatus, product, or process disclosed, or represents that its use would not infringe privately owned rights. Reference herein to any specific commercial product, process, or service by trade name, trademark, manufacturer, or otherwise, does not necessarily constitute or imply its endorsement, recommendation, or favoring by the United States Government or any agency thereof or its contractors or subcontractors. The views and opinions of authors expressed herein do not necessarily state or reflect those of the United States Government or any agency thereof.

# Underpotential Deposition of 3d Transition Metals: Versatile Electrosynthesis of Single-Atom Catalysts on Oxidized Carbon Supports

---

Aidan Francis Meese<sup>±</sup>, Cade Napier<sup>±</sup>, David J. Kim<sup>±</sup>, Kali Rigby<sup>±</sup>, Tayler Hedtke<sup>±</sup>, Denis Leshchev<sup>‡</sup>, Eli Stavitski<sup>‡</sup>, Lucas R. Parent<sup>§</sup>, Jae-Hong Kim<sup>\*±</sup>

<sup>±</sup> *Department of Chemical & Environmental Engineering, Yale University, New Haven, CT 06520, United States*

<sup>‡</sup> *National Synchrotron Light Source II, Brookhaven National Laboratory, Upton NY, 11973*

<sup>§</sup> *Innovation Partnership Building, University of Connecticut, 159 Discovery Dr., Storrs, CT, 06269 USA*

*\* Corresponding author*

## Abstract

Use of single-atom catalysts (SACs) has become a popular strategy for tuning activity and selectivity towards specific pathways. However, conventional SAC synthesis methods require high temperatures and pressures, complicated procedures, and expensive equipment. Recently, underpotential deposition (UPD) has been investigated as a promising alternative, yielding high-loading SAC electrodes under ambient conditions and within minutes. Yet only few studies have employed UPD to synthesize SACs, and all have been limited to UPD of Cu. In this work, we report a flexible UPD approach for synthesis of mono- and bi-metallic Cu, Fe, Co, and Ni SACs directly on oxidized, commercially available carbon electrodes. We investigate the UPD mechanism using in-situ x-ray absorption spectroscopy and, finally, assess the catalytic performance of a UPD-synthesized Co SAC for electrochemical nitrate reduction to ammonia. Our findings expand upon the usefulness and versatility of UPD for SAC synthesis, with hopes of enabling future research towards realization of fast, reliable, and fully electrified SAC synthesis processes.

## Data Availability Statement

Source data pertaining to the figures included in this manuscript and/or its supporting information are available upon reasonable request.

## Conflict of Interest Disclosure

The authors of this manuscript declare to have no competing conflicts of interest related to this work.

## 33 1. Introduction

---

34 Single-atom catalysts (SACs) have attracted attention across a range of disciplines in catalysis,  
35 owing to their unique, unsaturated coordination environments and strong metal-substrate  
36 interactions.<sup>1-6</sup> Yet, reliable synthesis of SACs remains challenging due to the high surface free  
37 energy of isolated metal atoms, which favors aggregation under conditions of typical syntheses  
38 and applications.<sup>7-8</sup> A variety of synthesis techniques have been developed in the literature, but  
39 many leading methods require the use of high temperature and pressure,<sup>9-14</sup> inert gas  
40 environment,<sup>15-18</sup> and/or expensive equipment,<sup>19-21</sup> as well as lengthy procedures and reaction  
41 times.

42 Electrochemical approaches to SAC synthesis offer a promising alternative, since they can  
43 be performed under ambient conditions and on the scale of minutes.<sup>22-24</sup> However, the large  
44 overpotentials at which electrodeposition is typically performed render it difficult to prevent  
45 formation of metal-metal bonds.<sup>25-26</sup> To address this problem, Xia et al. were the first to explore  
46 the use of underpotential deposition (UPD) for “self-terminating” synthesis of Cu SACs.<sup>23</sup> Unlike  
47 traditional electrodeposition, UPD is performed at potentials positive of or equal to a metal  
48 precursor’s standard reduction potential (SRP), *i.e.*, where reductive formation of metal-metal  
49 bonds is thermodynamically forbidden. Instead, metal atoms undergo electrosorption and/or  
50 reduction onto suitable anchor-sites of the substrate, such as nonmetal dopants, lattice defects, and  
51 vacancies.<sup>27-28</sup>

52 UPD of one metal onto a foreign metal substrate (*i.e.*, a bulk metal electrode) has been a  
53 subject of research for decades, finding use in niche applications such as stripping voltammetry  
54 and electroplating.<sup>29-33</sup> However, few publications have applied UPD as a strategy for synthesis of  
55 SACs supported on non-metal substrates. These include the synthesis of Cu SACs supported on  
56 transition metal dichalcogenides followed by galvanic displacement of Cu with noble metals,<sup>23</sup>  
57 and the synthesis of copper SACs on sulfur-doped graphite foam.<sup>34</sup> While these studies  
58 demonstrate the promise of UPD-based strategies for synthesis of Cu SACs, questions remain as  
59 to the precise mechanism of UPD on non-metal substrates and its ability to form SACs of metals  
60 less noble than Cu.

61 In this work, we present a versatile, one-step UPD-based SAC synthesis protocol to deposit a  
62 variety of transition metals, *e.g.*, Cu, Fe, Co, and Ni directly onto oxidized carbon electrodes,  
63 without use of inks or binders (**Figure 1a**). We then extend this protocol for the first time to obtain  
64 bi-metallic SACs and employ a combination of electrochemical techniques, x-ray photoelectron  
65 spectroscopy (XPS), and ex- and in-situ x-ray absorption spectroscopy (XAS) to track the  
66 coordination environment of Cu atoms through the course of UPD. Lastly, to showcase the  
67 performance of our transition metal SACs, we employ a Co-based SAC for electrochemical nitrate  
68 reduction to ammonia, a promising alternative to the energy-intensive Haber-Bosch process.

## 69 2. Results and Discussion

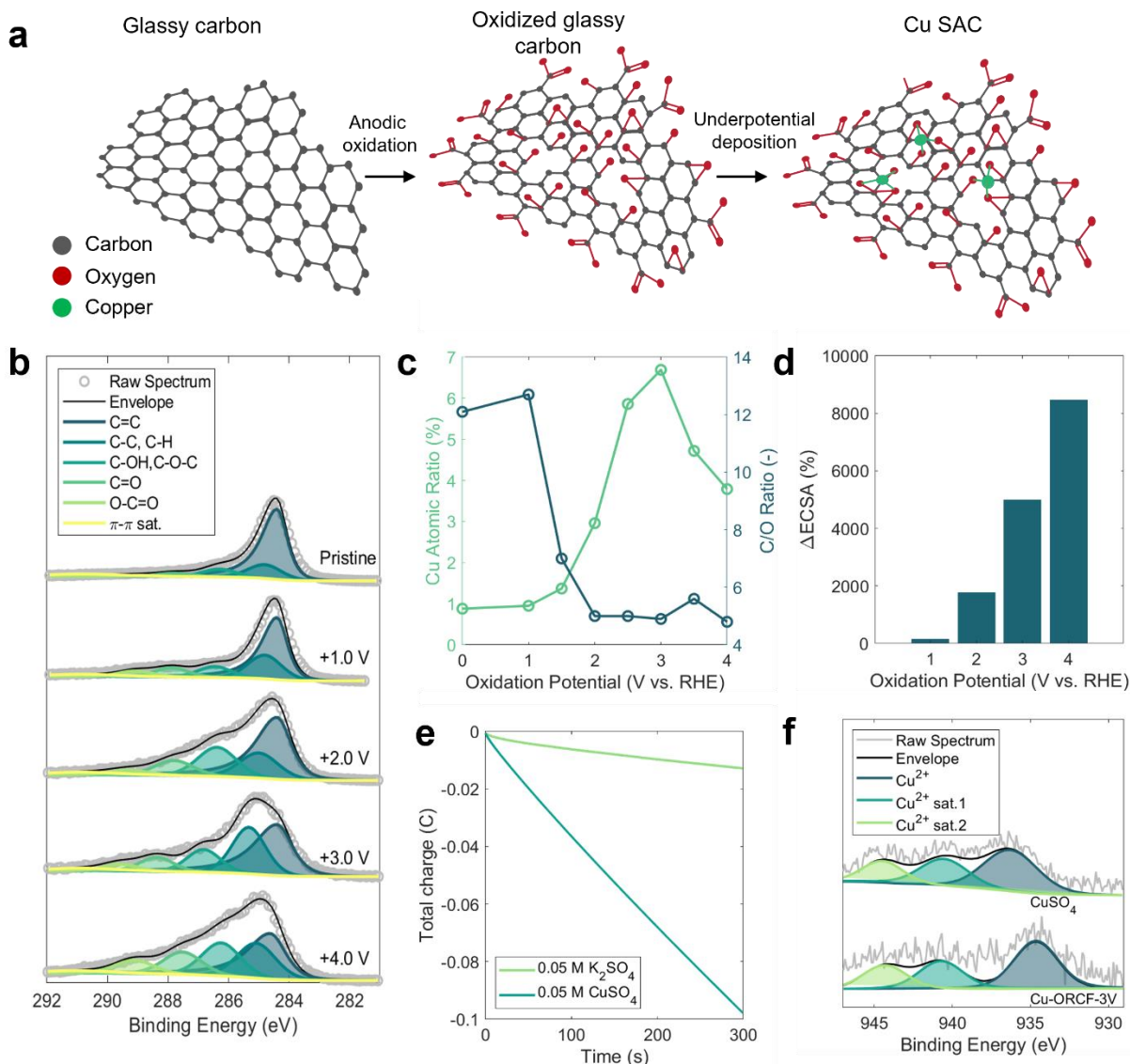
---

70 **Functionalization of oxidized carbon supports.** Carbon-based electrode materials are favored in  
71 numerous applications owing to their tunable morphologies, good conductivity, and low costs.  
72 Accordingly, we selected reticulated carbon foam (RCF), a porous carbon electrode material with

73 high surface-area-to-volume ratio,<sup>35</sup> as model electrode material and SAC support. Prior to SAC  
74 synthesis, the RCF was modified via electrochemical oxidation to increase electrochemically  
75 active surface area (ECSA) and abundance of single-atom anchor-sites, such as oxygen-containing  
76 functional groups as well as lattice vacancies and defects.<sup>36-38</sup> Direct modification and use of RCF  
77 as base electrode and SAC support eliminates the need for attachment of catalyst/substrate via  
78 drop-casting or otherwise. The extent of oxidation was controlled by varying the applied potential  
79 from +1.0 V to +4.0 V vs. RHE.

80 Comparison of XPS C1s regions for pristine RCF and ORCF-x (oxidized RCF, where x  
81 represents oxidation potential) confirms successful functionalization of RCF with oxygen-  
82 containing moieties (**Figure 1b**) The peak distribution for pristine RCF resembles typical sp<sup>2</sup>  
83 carbon,<sup>39</sup> with a dominant C=C peak and small contributions from oxygen-containing moieties.  
84 Following oxidation, peaks corresponding to oxygen-functionalized carbon, particularly C–OH,  
85 O–C–O, and C=O moieties, become markedly more prominent. C/O ratios for each sample exhibit  
86 a similar trend, ranging from 12.1 in pristine RCF to 4.8 in ORCF-4V (**Figure 1c, Table S1**).

87 In addition to oxygen-containing functional groups, we observed changes to both ECSA  
88 and carbon defect level in ORCF following oxidation. Double layer capacitance (DLC)  
89 measurements revealed a trend of dramatically increased ECSA with increasing oxidation potential  
90 (**Figure 1d, Figure S1**), illustrated by an ~80-fold increase in ECSA of ORCF-4V over pristine  
91 RCF. Interestingly, by comparison of D and G band intensities (*i.e.*, I<sub>D/G</sub> ratio) in the Raman spectra  
92 of each sample (**Figure S2**), we found no evidence of an increase in defect level following  
93 oxidation. In fact, due to the amorphous structure of reticulated carbon, pristine RCF demonstrates  
94 a relatively high D/G ratio of ~1.15, which appears to decrease following the oxidation at potentials  
95 +3.0 V and greater. This may be due to excessive oxidation of the carbon support, which can result  
96 in evolution of CO<sub>2</sub>(g) and delamination of defect-rich graphite layers.<sup>40</sup> Nevertheless, the higher  
97 Cu content of ORCF-3V (now referred to as ORCF) following UPD (**Figure 1c, Supplementary**  
98 **Note 1, Figures S3-S4, Table S2**) led us to select +3.0 V as the oxidation potential for subsequent  
99 investigation.



101

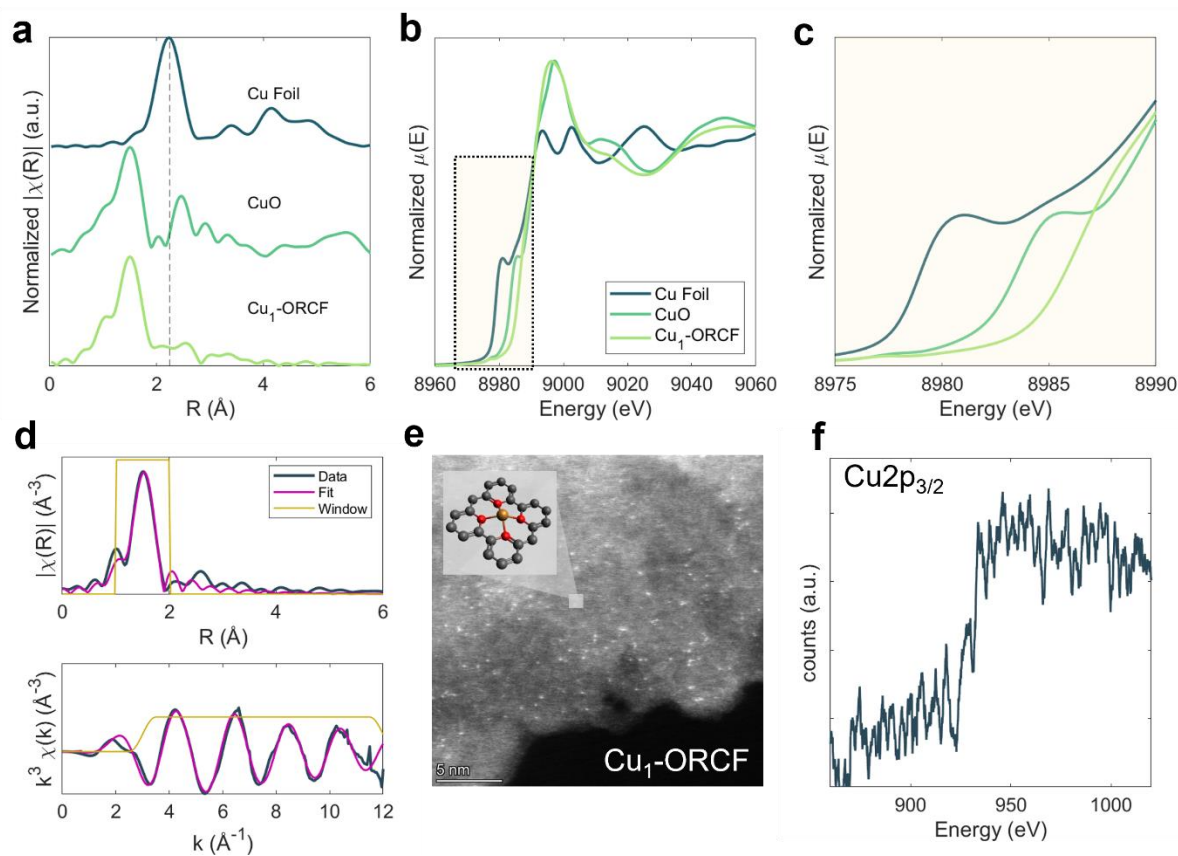
102 **Figure 1.** Overview of SAC synthesis approach and characterization of oxidized carbon substrates. (a) illustration of  
 103 key steps in UPD-based SAC synthesis approach; (b) Normalized C1s XPS spectra of pristine RCF and ORCF  
 104 substrates (key entries are in descending order from low to high binding energy). Six peaks were fitted to each C1s  
 105 spectrum, corresponding to C=C (248.5 eV), C-C, C-H (285.0 eV), C-OH, C-O-C (286.5 eV), C=O (287.9 eV),  
 106 O-C=O (288.8 eV), and  $\pi$ - $\pi^*$  satellite (291.6 eV);<sup>41</sup> (c) Relative Cu atomic ratio and C/O ratio of RCF and ORCF  
 107 substrates as functions of oxidation potential, estimated using XPS; (d) Change in ECSA for ORCF substrates  
 108 following oxidation at various potentials, as determined from DLC measurements (e) Coulometric curves for ORCF-  
 109 3V in 0.050 M  $CuSO_4$  and 0.05 M  $K_2SO_4$ , respectively; (f) Normalized, deconvoluted XPS  $Cu2p_{3/2}$  spectra of UPD  
 110 Cu-ORCF-3V and  $CuSO_4$ -ORCF-3V.

111 **Synthesis and Characterization of Cu-ORCF SAC.** As a starting point for developing a protocol  
 112 for a more universal UPD synthesis strategy, we investigated UPD of Cu SACs on ORCF. Cu is  
 113 well-suited for reductive electrochemical synthesis owing to its SRP of +0.34 V ( $Cu^{2+} + 2e^- \rightarrow$   
 114  $Cu^0$ ),<sup>42</sup> situated positive of the competing hydrogen evolution reaction (HER:  $2H^+ + 2e^- \rightarrow H_2$   
 115 (g)).<sup>43</sup> Moreover, unlike noble metals such as Pd and Pt,  $Cu^{2+}$  is readily soluble as a hydrated cation

116 in neutral and acidic electrolytes,<sup>44</sup> avoiding the added complexity of ligands such as Cl<sup>-</sup> and NH<sub>3</sub>  
117 in the deposition process.

118 Previous works investigating UPD for SAC synthesis employ cyclic voltammetry (CV) of  
119 the support material in precursor-containing electrolyte to select an appropriate potential for UPD  
120 ( $E_{\text{UPD}}$ ).<sup>23, 34</sup> The success of this approach, however, depends on the homogeneity of the substrate  
121 surface, as well as its DLC, which may affect the sharpness and intensity of redox peaks above the  
122 background current.<sup>45</sup> Thus, heterogeneous substrate materials, possessing large ECSA and  
123 various single-atom anchor-sites, are unlikely to exhibit peaks corresponding to UPD  
124 phenomena.<sup>27</sup> In fact, a CV of ORCF in 0.05 M CuSO<sub>4</sub> (**Figure S5**) shows no peaks attributable  
125 to Cu UPD. Rather, we postulate that by applying a constant potential close to but positive of a  
126 metal precursor's SRP (*i.e.*, approaching its equilibrium potential), a high surface coverage of  
127 metal atoms can be achieved without formation of metal-metal bonds. To assess this hypothesis,  
128 we performed chronoamperometry (CA) on ORCF in Ar-saturated 0.05 M CuSO<sub>4</sub> at  
129 underpotentials of 200, 100, 50, and 25 mV relative to the Cu<sup>2+</sup>/Cu<sup>0</sup> SRP, respectively (**Figure**  
130 **S6**). The increase in magnitude of total charge passed as the deposition potential is shifted closer  
131 to the Cu<sup>2+</sup>/Cu<sup>0</sup> SRP suggests an increase in extent of Cu UPD. Thus, to achieve a high loading of  
132 isolated Cu atoms on ORCF while remaining safely positive of the Cu<sup>2+</sup>/Cu<sup>0</sup> SRP, we selected an  
133 underpotential of 25 mV for further experiments.

134 To investigate the mechanism of Cu deposition, we performed CA experiments on ORCF  
135 working electrodes in blank (0.05 M K<sub>2</sub>SO<sub>4</sub>) and test (0.05 M CuSO<sub>4</sub>) electrolytes. The resulting  
136 coulometric curves (**Figure 1e**) show that substantially more charge is passed in the presence of  
137 CuSO<sub>4</sub>, suggesting that a reductive process involving Cu<sup>2+</sup> has occurred. To further verify that Cu  
138 undergoes a Faradaic change during deposition (as opposed to physisorption alone), we performed  
139 XPS (**Figure 1f**) of UPD Cu-ORCF and ORCF with drop-casted CuSO<sub>4</sub> electrolyte (without any  
140 further treatment). The ~2 eV shift of the primary Cu<sup>2+</sup> peak towards lower binding energy in UPD  
141 Cu-ORCF is likewise suggestive of a change in chemical state following UPD.



142

143 **Figure 2.** XAS and STEM characterization of Cu<sub>1</sub>-ORCF. (a) Comparison of FT-EXAFS, (b) full XANES region  
 144 (shaded region represents approximately the axes limits of the pre-edge region enlarged in panel c), (c) and pre-edge  
 145 only for Cu<sub>1</sub>-ORCF and Cu standards; (d) Fitted Cu K-edge FT-EXAFS (top) and EXAFS (bottom) of Cu<sub>1</sub>-ORCF;  
 146 (e) Atomic-resolution HAADF-STEM image (scale bar is 5 nm) and graphical rendering of one plausible metal-site  
 147 coordination structure of Cu<sub>1</sub>-ORCF; (f) Cu<sub>2p<sub>3/2</sub></sub> regional EELS spectrum collected over a small region of Cu<sub>1</sub>-ORCF  
 148 containing multiple bright spots.

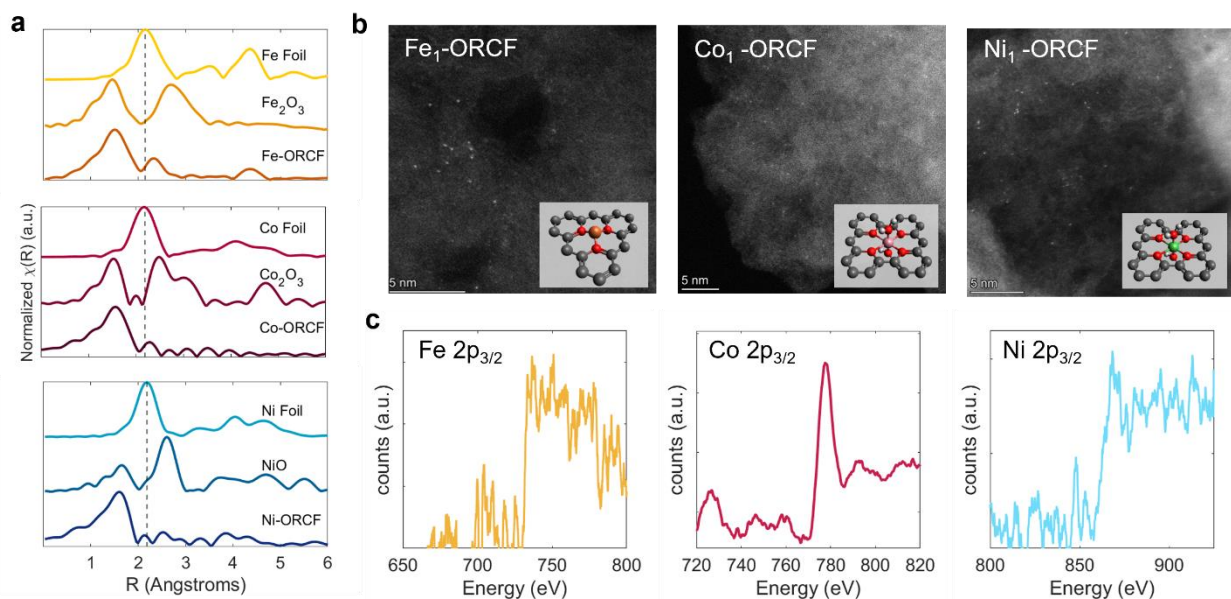
149 We assessed atomic dispersion of Cu by evaluating the coordination environment of Cu-  
 150 ORCF via XAS analysis. The Fourier transform (FT)-EXAFS region of Cu-ORCF (**Figure 2a**)  
 151 contains a single peak at  $\sim 1.6$  Å, which aligns with the first shell Cu-O peak observed in CuO. The  
 152 absence of any metal-metal peak, as observed at  $\sim 2.3$  Å in Cu foil, suggests that Cu sites in Cu-  
 153 ORCF are atomically dispersed.<sup>46</sup> The Cu K-edge XANES (**Figure 2b, 2c**) shows an edge position  
 154 and white-line intensity close to but higher than the CuO standard, suggesting an oxidation state  
 155 slightly greater than +2.<sup>47</sup> This unusually high valence state of Cu<sub>1</sub> may result from the highly  
 156 oxidized ORCF substrate, which provides an abundance of electron-withdrawing oxygen atoms  
 157 that may coordinate with metal adatoms.<sup>48</sup> Note, however, that this high final oxidation state  
 158 indicates that no net reduction occurs during the deposition of the precursor ion, which is initially  
 159 in an oxidation state of +2. Thus, the UPD mechanism taken by Cu atoms in this work appears to  
 160 differ from the more well-defined UPD of metals onto foreign metal substrates, in which the  
 161 deposited metal tends to be reduced to a near-zero valent state.<sup>28</sup> Examination of the pre-edge  
 162 features of UPD Cu-ORCF (**Figure 2c**) reveals a small peak at  $\sim 8977$  eV corresponding to dipole-  
 163 forbidden  $1s \rightarrow 3d$  transition, also indicative of Cu<sup>2+</sup> species.<sup>49</sup> Interestingly, the *k*- and *R*-space

164 fitting of Cu-ORCF FT-EXAFS (**Figure 2d**) yielded an average coordination number (CN) of 3.8  
165 (**Table S3**) despite the lack of a pre-edge peak at 8985 eV, which is typically present in tetra-  
166 coordinated Cu species.<sup>50</sup> However, the low intensity of the 1s→3d transition peak is more in-line  
167 with tetra-coordinated Cu species (*e.g.*, CuO) than penta- or hexa-coordinated species (*e.g.*,  
168 Cu<sup>2+</sup><sub>(aq)</sub>).<sup>51</sup> This may suggest that Cu atoms in Cu<sub>1</sub>-ORCF have a distorted square-planar or  
169 tetrahedral configuration (inset of **Figure 2e**).

170 Atomic-resolution images taken via high-angle annular dark field scanning transmission  
171 electron microscopy (HAADF-STEM) of Cu-ORCF depict isolated high-Z atoms dispersed across  
172 the sample surface, with no obvious signs of metallic clusters or nanoparticles (**Figure 2e, Figure**  
173 **S7**). Electron energy loss spectroscopy (EELS) of a limited region of the sample (ca. 3 nm × 3 nm)  
174 containing multiple, dynamic atoms (**Figure S8**) reveals an edge at ~930 eV (**Figure 2f, Figure**  
175 **S9**), corresponding to the binding energy of the Cu 2p<sub>3/2</sub> orbital. This confirms that the high-Z  
176 atoms observed in the HAADF-STEM images correspond to isolated Cu atoms on the ORCF  
177 substrate. The weight loading of Cu in Cu<sub>1</sub>-ORCF was determined to be 0.36 ± 0.061 % (**Table**  
178 **S4**).

179 **UPD Synthesis of Other 3d Transition Metal SACs.** The data presented in the preceding sections  
180 provide strong evidence of successful synthesis of a Cu SAC supported on ORCF (now referred  
181 to as Cu<sub>1</sub>-ORCF) by our UPD approach. Inspired by the rapid timescale and simplicity of UPD for  
182 Cu SAC synthesis, we sought to expand this approach to synthesize SACs consisting of Fe, Co,  
183 and Ni supported on ORCF. We hypothesized that it would be possible to obtain morphologically  
184 similar SACs by adjusting only the E<sub>UPD</sub> and identity of metal precursor. For each metal, E<sub>UPD</sub> was  
185 selected following the same rationale as described previously for Cu<sub>1</sub>-ORCF. **Table S5**  
186 summarizes the half-reaction, SRP, and selected E<sub>UPD</sub> for each metal investigated. FT-EXAFS of  
187 Fe, Co, and Ni K-edge spectra confirms successful synthesis of Fe<sub>1</sub>-ORCF, Co<sub>1</sub>-ORCF, and Ni<sub>1</sub>-  
188 ORCF, respectively (**Figure 3a**), evidenced by strong metal-oxide peaks and the absence of metal-  
189 metal peaks. As in the case of Cu<sub>1</sub>-ORCF, Fe, Co, or Ni K-edge XANES of each respective  
190 material (**Figures S10a-b, S11a-b, S12a-b**) exhibit white-line intensities close to those of 2+ or  
191 3+ metal oxide standards. The *k*- and *R*-space fitting of each catalyst yielded CNs of 3.6, 6.6, and  
192 5.6 for Fe, Co, and Ni, respectively (**Figures S10c-d, S11c-d, S12c-d**), suggesting that Cu and Fe  
193 tend to form tetracoordinated configurations, while Co and Ni favor hexacoordinated octahedral  
194 configurations. This observation aligns well with the theory of crystal field stabilization energies  
195 for transition metal complexes; as d<sup>7</sup> and d<sup>8</sup> transition metals, respectively, Co and Ni tend to have  
196 higher octahedral site preferences than Cu or Fe. Due to the strict geometric constraints of a  
197 saturated octahedral coordination sphere, however, it seems unlikely that all Co and Ni atoms in  
198 Co<sub>1</sub>- and Ni<sub>1</sub>-ORCF share bonds with only O-atoms of the substrate. We instead propose a  
199 hexacoordinated model in which each Co or Ni atom shares 4-6 bonds with O-containing groups  
200 of the substrate and 1-2 bonds to water ligands leftover from the precursor ion's coordination  
201 sphere (see insets of **Figure 3b**). We emphasize, however, that each of these modeled coordination  
202 environments present only one plausible configuration for the metal sites, while the highly  
203 disordered nature of oxidized carbon substrates implies that a variety of configurations may be  
204 possible. HAADF-STEM images of each metal show similar bright spots dispersed on ORCF, with  
205 no obvious signs of nanoparticles or metallic clusters (**Figure 3b, Figures S13-S15**). Scanning

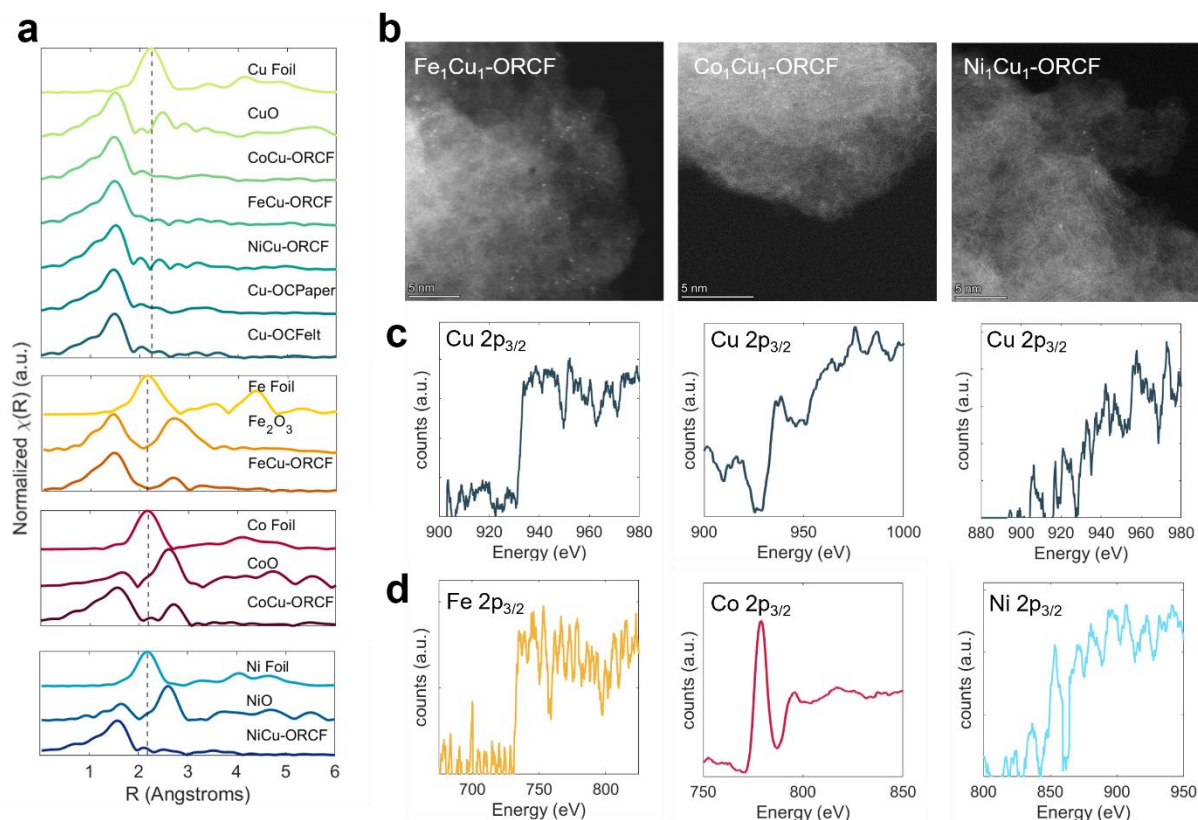
206 EELS was performed over small sections (ca. 3 nm x 3nm) of each sample (**Figure 3c, Figures**  
 207 **S16-S18**) revealing edges corresponding to the  $2p_{3/2}$  orbitals of each metal. Although the presence  
 208 of hydrogen bubbles and activated hydrogen on the ORCF substrate may impact the overall  
 209 efficiency of metal deposition, the cooccurrence of HER with UPD of Fe, Co, and Ni does not  
 210 appear to affect the morphology of the resulting SAC.



211  
 212 **Figure 3.** XAS and STEM/EELS characterization of additional monometallic transition metal SACs. **(a)** Co, Fe, and  
 213 Ni K-edge FT-EXAFS **(b)** HAADF-STEM images (scale bars = 5 nm) and graphical renderings of plausible metal-  
 214 site coordination structures, and **(c)** regional EELS spectra of  $Fe_1$ -ORCF,  $Co_1$ -ORCF, and  $Ni_1$ -ORCF, respectively.

215 **UPD Synthesis of Bimetallic SACs.** Bimetallic SACs present exciting opportunities for  
 216 incorporating two distinct metal active sites into a single catalyst material.<sup>52</sup> The proximity of these  
 217 atomically dispersed metal sites to one another has been shown to enable synergistic effects,  
 218 resulting in improved catalytic performance over either metal alone.<sup>53-55</sup> For example, Fu, et al.,  
 219 demonstrated improved performance of a bimetallic Ir-Mo SAC for selective reduction of 4-  
 220 nitrostyrene (4-NS), owing to synergy between  $H_2$  activating  $Ir_1$  sites and preferential adsorption  
 221 of 4-NS at  $Mo_1$  sites.<sup>54</sup> Following successful synthesis of  $Cu_1$ -,  $Fe_1$ -,  $Co_1$ -, and  $Ni_1$ -ORCF catalysts,  
 222 we sought to produce randomly interspersed bimetallic SACs by applying sequential UPD steps  
 223 in separate electrolytes. Following this strategy, we synthesized FeCu-, CoCu-, and NiCu-ORCF  
 224 SACs by depositing Fe, Co, or Ni onto freshly synthesized  $Cu_1$ -ORCF. In each case, Cu was  
 225 deposited first because of its positive reduction potential compared to the other metals (**Table S5**),  
 226 which prevents galvanic displacement of Cu atoms by less-noble Fe, Co, or Ni ions during the  
 227 second UPD step.<sup>23</sup> Cu, Fe, Co, and Ni K-edge FT-EXAFS and XANES for FeCu-ORCF, CoCu-  
 228 ORCF, and NiCu-ORCF resemble those of respective monometallic counterparts (**Figure 4a,**  
 229 **Figures S19-S21**). In addition to metal-oxide peaks and absence of metallic bonding, the spectra  
 230 show no evidence of bonding between the two metals deposited (*i.e.*, alloying) nor any other  
 231 noticeable influences of Fe, Co, or Ni on the Cu coordination environment. HAADF-STEM  
 232 images (**Figure 4b, Figures S22-24**) of FeCu-ORCF, CoCu-ORCF, and NiCu-ORCF depict  
 233 similar high-Z atoms dispersed on ORCF supports. EELS spectra (**Figure 4c-d, Figures S25-27**)

234 exhibit edges for both atomic species in each bimetallic sample, suggesting that the dispersed  
 235 single-atoms are a mixture of the two deposited metals. Identities of individual metal atoms were  
 236 not distinguishable via EELS due to low signal intensity at sub-atomic resolution and movement  
 237 of metal atoms under the incident electron beam.<sup>56</sup>

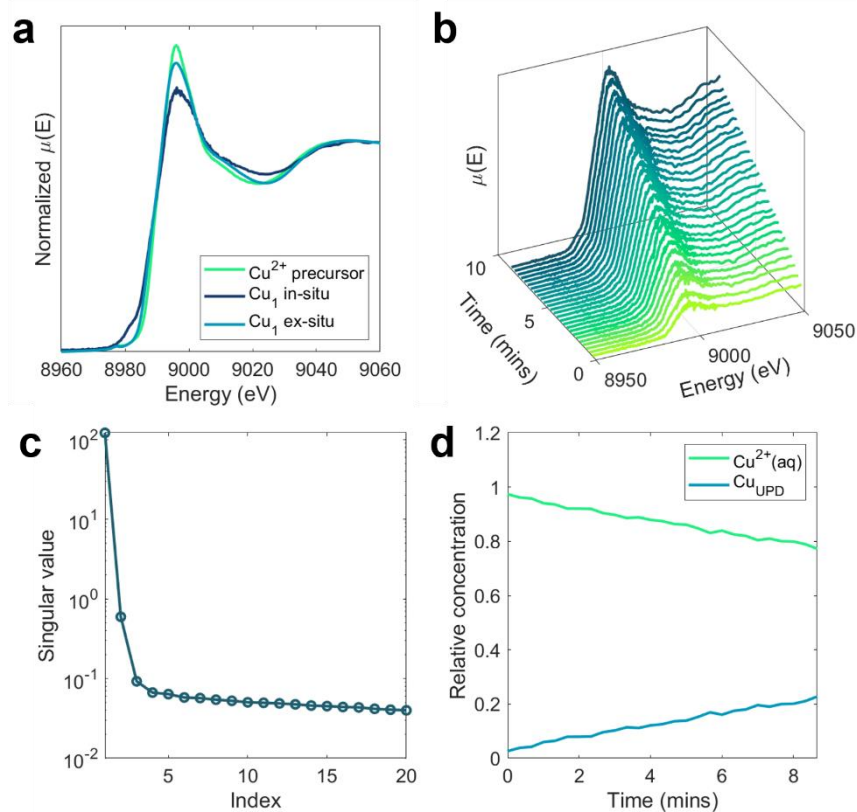


238  
 239 **Figure 4.** XAS and STEM/EELS characterization of bimetallic SACs and Cu SACs on additional substrates. **(a)** FT-  
 240 EXAFS of Cu, Fe, Co, and Ni K-edges for respective Cu and bimetallic SACs; **(b)** HAADF-STEM images (scale bars  
 241 = 5 nm), **(c)** Cu 2p<sub>3/2</sub> EELS edges, and **(d)** Fe, Ni and Co 2p<sub>3/2</sub> EELS edges of Fe<sub>1</sub>Cu<sub>1</sub>-, Co<sub>1</sub>Cu<sub>1</sub>- and Ni<sub>1</sub>Cu<sub>1</sub>-ORCF,  
 242 respectively.

243 **UPD of Cu on Additional Oxidized Carbon Substrates.** Although useful for fundamental  
 244 investigations into UPD-based SAC synthesis, the poor mechanical stability and high cost of RCF  
 245 limits its feasibility in practical applications. We therefore applied our synthesis methodology to  
 246 two additional commonly employed electrode materials, Sigracet carbon paper and carbon felt.  
 247 Sigracet carbon paper is a robust, highly porous electrode material consisting of interwoven carbon  
 248 fibers coated with a carbon black microporous layer, ideal for use in gas diffusion cells.<sup>57-59</sup> Carbon  
 249 felt consists of thread-like fibers of carbon which form a soft, flexible network of pores. It is  
 250 typically less dense and more hydrophilic than carbon paper and is well-suited for flow-through  
 251 applications.<sup>60</sup> Prior to UPD, each material was similarly oxidized at +3.0 V to introduce oxygen-  
 252 containing functional groups and increase ECSA. XPS C1s spectra of the oxidized materials  
 253 (denoted OCPaper and OCFelt, **Figures S28-S29**) show an abundance of oxygen-containing  
 254 functional groups. Cu UPD was performed on each material at an underpotential of 25 mV (vs.

255 Cu<sup>2+</sup>/Cu<sup>0</sup> SRP) to produce Cu-OCPaper and Cu-OCFelt. FT-EXAFS (**Figure 4a, Figures S30-31**)  
 256 and HAADF-STEM images (**Figures S32-S33**) of Cu-OCPaper and Cu-OCFelt confirmed atomic  
 257 dispersion of Cu in each material. These results underscore the versatility of UPD to produce SACs  
 258 supported on a range of commercial carbon-based electrode materials.

259 **In-Situ XAS of Cu UPD.** Although ex-situ characterization as discussed above can confirm  
 260 formation of atomically dispersed metal-substrate bonds following UPD, it provides little  
 261 information on the metal's coordination environment *during* UPD. Thus, we performed in-situ  
 262 XAS to track transformation of Cu atoms from aqueous ions to oxygen-coordinated single-atoms  
 263 under UPD conditions (see **Methods** for experimental details). At open circuit potential (OCP),  
 264 prior to application of E<sub>UPD</sub>, a strong background signal corresponding to hydrated Cu<sup>2+</sup> (**Figure**  
 265 **5a**) near the electrode was observed and remained unchanged over a 5-minute period. Following  
 266 application of E<sub>UPD</sub>, we observed slight changes in the total signal, including reduction in white-  
 267 line intensity and growth of a small pre-edge peak at 8980 eV, which we attribute to formation of  
 268 Cu<sub>1</sub> bonds with surface-bound oxygen groups on the electrode.



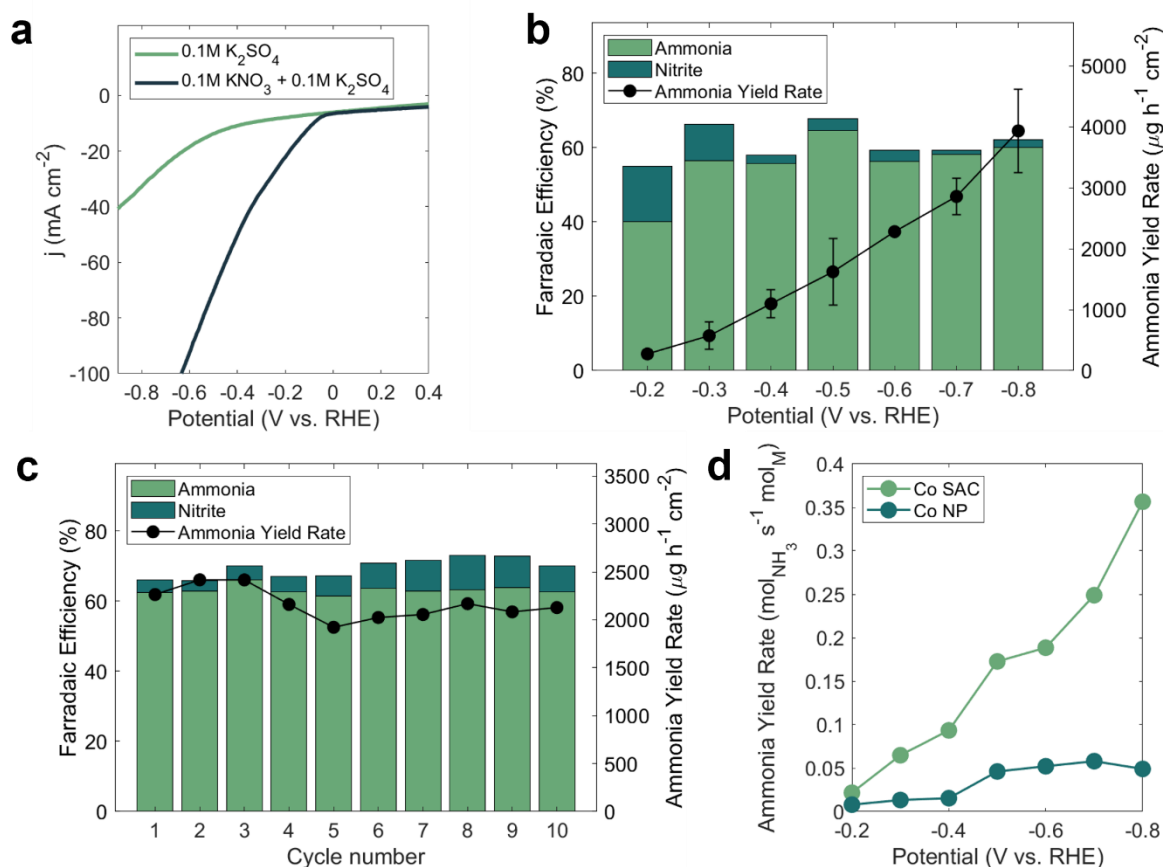
269  
 270 **Figure 5.** In-situ XAS and singular value decomposition (SVD) of an oxidized carbon paper electrode during Cu  
 271 UPD. **(a)** Cu K-edge XANES of the electrode in Cu electrolyte, but prior to application of potential  
 272 (adsorbed/dissolved Cu<sup>2+</sup> precursor only), under the applied UPD potential (in-situ), and in air after drying (ex-situ);  
 273 **(b)** non-normalized, background subtracted Cu K-edge XANES of the oxidized carbon paper electrode during UPD;  
 274 **(c)** singular values of the first 20 computed spectral components; **(d)** relative concentrations of Cu<sup>2+</sup>(aq) and the  
 275 underpotentially deposited Cu<sub>1</sub> species.

276 Subtraction of the background  $\text{Cu}^{2+}$  signal collected at OCP enabled us to isolate the  
277 component spectra of this newly formed species (**Figure 5a**), which appeared following the first  
278 scan at  $E_{\text{UPD}}$  and continued to grow in intensity throughout the 10-minute experiment (**Figure 5b**).  
279 Analysis of the total spectra via singular value decomposition (SVD) confirmed that only two  
280 spectral components were present throughout the experiment (**Figure 5c, Supplementary Note**  
281 **S2**). Fitting the spectral series with the extracted spectra of newly formed species and the hydrated  
282  $\text{Cu}^{2+}$  allowed us to estimate their relative concentrations (**Figure 5d**). Interestingly, the spectrum  
283 of  $\text{Cu}_1$  formed in-situ ( $\text{Cu}_1$ -in-situ) differs from that of  $\text{Cu}_1$ -ex-situ, obtained after air-drying of the  
284 electrode. While  $\text{Cu}_1$ -ex-situ exhibits mostly  $\text{Cu}^{2+}$  character,  $\text{Cu}_1$ -in-situ possesses notably more  
285  $\text{Cu}^+$  character, evidenced by its diminished white-line intensity and pre-edge peak ca. 8980 eV.<sup>61</sup>  
286 This suggests that UPD may proceed via reduction of  $\text{Cu}^{2+}_{(\text{aq})}$  to a partially reduced intermediate  
287 Cu-O species which, upon air-exposure, reconfigures to an oxidation state of approximately +2.  
288 In addition to providing insight on the timescale of SAC formation via UPD, this finding may  
289 underscore the importance of electron-rich anchor-sites (*e.g.*, oxygen atoms) in facilitating  
290 reduction of  $\text{Cu}^{2+}_{(\text{aq})}$  to form stable metal-substrate bonds during UPD.

291 **Electrochemical Nitrate Reduction to Ammonia.** SACs have demonstrated excellent  
292 performance for selective reduction of nitrate to ammonia, often displaying higher  $\text{NH}_3$  Faradaic  
293 efficiency (FE) and intrinsic activity compared to nanostructured counterparts.<sup>61-64</sup> Cu is typically  
294 considered the benchmark catalyst for electrochemical nitrate reduction to ammonia ( $\text{NO}_3\text{R}$ ),  
295 owing to its high activity for the rate limiting step of  $\text{NO}_3^-$  to  $\text{NO}_2^-$  and its relatively weak  
296 interaction with hydrogen, which inhibits the competing HER reaction.<sup>63, 65</sup> However, recent  
297 studies have reported exceptional performance of Co-based catalysts attributed to formation of  
298 active hydrogen on Co active-sites, which boosts ammonia selectivity by mediating the efficient  
299 transfer of H-atoms to the central N-atom of intermediate species.<sup>64, 66</sup> Inspired by these findings,  
300 we selected  $\text{Co}_1$ -OCPaper as a model  $\text{NO}_3\text{R}$  catalyst to showcase the performance of our UPD-  
301 synthesized SACs.

302 As an initial screening of the catalytic performance of  $\text{Co}_1$ -OCPaper for  $\text{NO}_3\text{R}$ , linear sweep  
303 voltammetry (LSV) was performed in Ar-saturated electrolytes containing nitrate (0.1 M  $\text{KNO}_3$  +  
304 0.1 M  $\text{K}_2\text{SO}_4$ , pH 11.5) and supporting electrolyte only (0.1 M  $\text{K}_2\text{SO}_4$ , pH 11.5, **Figure 6a**). The  
305 dramatic increase in current density in the presence of  $\text{KNO}_3$ , starting at an onset potential of -0.1  
306 V, suggests high selectivity of  $\text{Co}_1$ -OCPaper for reduction of  $\text{NO}_3^-$  over background HER.  
307 Electrocatalytic performance was further assessed via 1-hour batch experiments at fixed potentials  
308 from -0.2 to -0.8 V in 0.1 M  $\text{KNO}_3$  + 0.1 M  $\text{K}_2\text{SO}_4$  (**Figure 6b**), following which  $\text{NH}_3$  and  $\text{NO}_2^-$   
309 products were quantified using UV-vis spectrophotometry (see **Methods, Figures S34-S35**). The  
310 results show a steady increase in  $\text{NH}_3$  yield rate, from 280  $\mu\text{g h}^{-1} \text{cm}^{-2}$  at -0.2 V to 3900  $\mu\text{g h}^{-1} \text{cm}^{-2}$   
311 at -0.8 V, as the potential is shifted to more negative values. Meanwhile,  $\text{NH}_3$  selectivity (herein  
312 used interchangeably with FE) rose from 40% at -0.2 V to 64% at -0.5 V, remaining consistently  
313 >55% for all potentials -0.3 V and more negative. Production of  $\text{NO}_2^-$  remained low (1-10% of  
314 total FE) across all potentials (**Figure 6b**). Based on previous literature elucidating the critical role  
315 of  $\text{H}^*$  in facilitating the reduction of  $\text{NO}_3^-$  to  $\text{NH}_3$  over Co-based catalysts,<sup>66-67</sup> we attribute the  
316 strong catalytic performance of  $\text{Co}_1$ -OCPaper to the controlled production of  $\text{H}^*$  by Co active sites  
317 and their ability to rapidly transfer  $\text{H}^*$  to  $\text{NO}_3^-$ .

318 Co<sub>1</sub>-OCPaper demonstrated reasonable stability over 10, 1-hour cycles at -0.5 V (**Figure 6c**),  
 319 sustaining an NH<sub>3</sub> selectivity of >60% and yield rate of ~1500 μg h<sup>-1</sup> cm<sup>-2</sup>. No major differences  
 320 were observed in FT-EXAFS of Co<sub>1</sub>-OCPaper before and after the repeated cycling (**Figure S36**).  
 321 **Figure 6d** contrasts the NO<sub>3</sub>R performance of Co<sub>1</sub>-OCPaper with that of a Co-nanoparticle catalyst  
 322 supported on OCPaper (Co<sub>NP</sub>-OCPaper, characterization in **Figures S37-38**). The larger Co-mass-  
 323 normalized NH<sub>3</sub> yield rate of Co<sub>1</sub>-OCPaper across the entire potential range reflects the higher  
 324 intrinsic activity of Co single-atom sites compared to Co<sub>NP</sub>-OCPaper, and is in accordance with  
 325 previous studies comparing the performance of Fe-, Cu-, Co-, and Ru-based SACs to benchmark  
 326 nanoparticle catalysts.<sup>62-64</sup> These findings exemplify the catalytic performance of our UPD-  
 327 synthesized SACs for a relevant electrochemical application.



328 **Figure 6.** Electrochemical NO<sub>3</sub>RR performance of Co<sub>1</sub>-OCPaper ; **(a)** LSVs of Co<sub>1</sub>-ORCF in 0.1 M K<sub>2</sub>SO<sub>4</sub> and 0.1  
 329 M KNO<sub>3</sub> + 0.1M K<sub>2</sub>SO<sub>4</sub>, respectively; **(b)** NH<sub>3</sub> and NO<sub>2</sub><sup>-</sup> FE and NH<sub>3</sub> yield rate in 0.1 M KNO<sub>3</sub> + 0.1 M K<sub>2</sub>SO<sub>4</sub>,  
 330 measured following 1 h batch experiments at a range of potentials; **(c)** Performance of Co<sub>1</sub>-OCPaper in 0.1 M KNO<sub>3</sub>  
 331 + 0.1 M K<sub>2</sub>SO<sub>4</sub> over the course of 10 1-hour cycles at -0.5 V; **(d)** metal content-normalized ammonia yield rates of  
 332 Co<sub>1</sub>-OCPaper and Co<sub>NP</sub>-OCPaper.  
 333

### 334 3. Conclusions

335 Application of UPD towards SAC synthesis has been confined almost exclusively to Cu-based  
 336 catalysts on a narrow range of support materials, likely due to the analytical challenges posed by  
 337 substrate heterogeneity and co-occurrence of HER, which make it difficult to identify suitable  
 338 E<sub>UPD</sub>. In this work, by selecting E<sub>UPD</sub> based solely on a metal's SRP, we demonstrated for the first

339 time that UPD can be adapted to synthesize oxygen-bound SACs of 3d transition metals less-noble  
340 than Cu. In addition, we showed that UPD can be applied sequentially to obtain bimetallic SACs  
341 and performed directly onto commercial electrode materials, eliminating the need for inks or  
342 binders. These findings expand upon the usefulness and versatility of UPD for SAC synthesis,  
343 with hopes of enabling future research towards realization of fast, reliable, and fully electrified  
344 SAC synthesis processes.

345

346

## 347 **4. Methods**

---

### 348 **Materials**

349 All chemical reagents were purchased from Sigma-Aldrich (Missouri, USA) and were of ACS Reagent grade or  
350 higher. Reticulated carbon foam was purchased from Goodfellow Corporation (Pennsylvania, USA). Carbon paper  
351 (Sigracet 39BB) and carbon felt (AvCarb 100) were purchased from Fuel Cell Store (Colorado, USA).

### 352 **Preparation of oxidized carbon substrates**

353 Oxidized carbon substrates were prepared by electrochemical oxidation in an undivided, 3-electrode glass cell. A  
354 carbon rod (99.95% purity, Fischer) and Ag/AgCl electrode (sat. KCl, CH Instruments) were used as the counter and  
355 reference electrodes, respectively. In a typical procedure, 1 cm<sup>2</sup> of carbon-material working electrode (2 cm x 0.5 cm)  
356 was submerged in 0.1 M H<sub>2</sub>SO<sub>4</sub> and connected to a VSP-128 electrochemical workstation (Biologic, USA) using  
357 alligator clips. A fixed oxidative potential (+1.0 to +4.0 V) was applied for 300 s, after which the working electrode  
358 was removed and rinsed thoroughly with deionized water (18.2MΩ).

### 359 **UPD Synthesis of Cu SACs**

360 UPD experiments were performed in an undivided glass cell identical to that used for substrate oxidation. In a typical  
361 experiment 1 cm<sup>2</sup> of oxidized carbon working electrode (2 cm<sup>2</sup> total area) was submerged in Ar-saturated electrolyte  
362 containing 0.05 M CuSO<sub>4</sub> and 5 mM H<sub>2</sub>SO<sub>4</sub>. The system was left at open circuit potential (OCP) for 5 minutes prior  
363 to deposition to allow time for sorption of metal ions to take place on the electrode surface. Then, an underpotential  
364 of +25 mV (vs. Cu<sup>2+</sup>/Cu<sup>0</sup> SRP) was applied to the working electrode for a duration of 300 s. The as-obtained SAC  
365 electrode was removed from electrolyte and rinsed thoroughly with deionized water.

### 366 **UPD Synthesis of other transition metal SACs**

367 Fe, Co, and Ni SACs were synthesized following a similar procedure as in the case of Cu. In each case, an  
368 underpotential of +25 mV vs. the respective metal's SRP was applied for 300 s. Analogous electrolyte compositions  
369 were employed for each synthesis, namely combinations of 5 mM H<sub>2</sub>SO<sub>4</sub> with 0.05 M FeSO<sub>4</sub>, CoCl<sub>2</sub>, or NiNO<sub>3</sub>,  
370 respectively, to yield a 0.05 M solution of hydrated metal cation. Bimetallic SACs consisting of FeCu, CoCu, and  
371 NiCu, were obtained by depositing each metal in sequence, starting with the nobler metal (Cu) to avoid galvanic  
372 displacement.

### 373 **Electrochemical Synthesis of Co<sub>NP</sub>-OCPaper**

374 Co<sub>NP</sub>-OCPaper was prepared by reductive electrodeposition of Co onto as-prepared OCPaper substrate (oxidized at  
375 3.0 V for 300 s). Reaction conditions were kept identical to those used for synthesis of Co SACs, except that an  
376 overpotential of 0.5 V (vs. Co<sup>2+</sup>/Co<sup>0</sup> SRP) was applied to induce formation of Co-Co bonds.

### 377 **HAADF-STEM/EELS imaging and analysis**

378 Aberration corrected HAADF-STEM images and EELS spectra were obtained using an aberration corrected Titan  
379 Themis AC-STEM (ThermoFisher Scientific, USA) equipped with a Gatan Quanta GIF spectrometer (AMETEC, Inc.,  
380 USA) at the Thermo Fisher Scientific Center for Advanced Microscopy and Materials Analysis at UConn. The Themis  
381 was operated at 300 keV with a beam current of ca. 0.285 nA (spot size: 5, CLA aperture: 70 μm) for imaging and  
382 electron energy loss spectroscopy (EELS). Imaging was done using 130 mm camera length and the HAADF detector.  
383 For EELS, the 5 mm GIF aperture was used with a camera length of 21 mm ("Filtered" off, and "Descan" on) and a  
384 GIF dispersion of 0.1 or 0.25 eV/channel, depending on the sample. The GIF energy window was varied for each  
385 metal sample to contain the respective metal peak of interest and a sufficient pre-peak region for background  
386 subtraction. EELS spectra acquisition was done while the STEM beam was scanning over a ca. 3 nm x 3 nm square  
387 on the sample that contained metal atoms, and thus EELS spectra contained signal from all the single atoms within  
388 the scanning region.

### 389 **XAS measurements and data analysis**

390 XAS measurements were collected at Beamline 8-ID (ISS) of the National Synchrotron Light Source II located at  
391 Brookhaven National Laboratory, USA. The synchrotron's storage ring was operating at 3 GeV with a beam current  
392 of 400.1 mA. Measurements of Cu, Fe, Co, and Ni k-edges were acquired in fluorescence mode using a Si(111) double  
393 crystal monochromator and a passivated implanted planar silicon fluorescence detector at room temperature. For ex-  
394 situ measurements, samples were prepared either by grinding and casting as pellets using poly(ethylene glycol) as a  
395 binder (carbon foam, felt substrates) or by cutting and stacking of as-obtained electrodes (carbon paper substrates).  
396 All samples were placed into 12 mm sample holders and sealed with Kapton film. In-situ XAS experiments were  
397 performed under the same synthesis conditions as used in the preparation of ex-situ samples, except that a custom 3D-  
398 printed cell with 1 cm diameter Kapton tape window was used in place of a typical glass H-cell. All in-situ experiments  
399 were performed at room temperature with OCPaper as working electrode, plain carbon paper (Sigracet 39BB) as  
400 counter, and Ag/AgCl (sat. KCl) as reference. Collected spectra were processed and analyzed using Athena and  
401 Artemis software packages, including conversion of raw data to  $\mu(E)$ , background subtraction, normalization, Fourier  
402 Transform, and mathematical fittings.

### 403 **Additional materials characterization**

404 XPS data was collected using a monochromatic 1486.7 eV Al K $\alpha$  X-ray source on PHI VersaProbe II X-ray  
405 Photoelectron Spectrometer (Physical Electronics, USA). Raman spectroscopy was performed via Horiba LabRAM  
406 HR Evolution Raman spectrometer (Horiba Instruments, Japan). ICP-MS was performed using a Perkin Elmer ICP-  
407 MS Elan DRC-e (PerkinElmer, USA).

### 408 **Electrochemical Nitrate Reduction Experiments**

409 Nitrate reduction experiments were performed in batch mode in a standard 2-compartment H-cell divided by a Nafion  
410 117 cation exchange membrane (Fuel Cell Store, USA). Ag/AgCl (sat. KCl) and platinized Ti-mesh electrodes were  
411 used as reference and counter, respectively. An electrolyte consisting of 0.1 M KNO<sub>3</sub> + 0.1 M K<sub>2</sub>SO<sub>4</sub> was used as the  
412 test electrolyte, unless otherwise specified. Prior to use, electrolyte pH was adjusted to 11.5 by dropwise addition of  
413 1 M KOH solution to preempt the rapid change in pH caused by the consumption of H<sup>+</sup> during NO<sub>3</sub>RR. The cell was  
414 continuously sparged with high-purity Ar gas (99.995%) and left to equilibrate for 15 minutes prior to the application  
415 of potential. A fixed potential was then applied to the working electrode for a duration of 1hr under vigorous stirring  
416 (600 rpm) and continuous sparging with Ar.

### 417 **Quantification of Nitrate Reduction Products**

418 Quantification of ammonia and nitrite was performed via spectrophotometry using modified forms of the indophenol  
419 blue (ammonia) and Greiss (nitrite) methods, as reported in the work of Wu, et al.<sup>62</sup>

## 420 5. References

---

- 421  
422 1. Weon, S.; Huang, D.; Rigby, K.; Chu, C.; Wu, X.; Kim, J.-H., *ACS ES&T Engineering* **2021**, 1 (2), 157-  
423 172.
- 424 2. Ding, S.; Hülsey, M. J.; Pérez-Ramírez, J.; Yan, N., *Joule* **2019**, 3 (12), 2897-2929.
- 425 3. Kaiser, S. K.; Chen, Z.; Faust Akl, D.; Mitchell, S.; Pérez-Ramírez, J., *Chemical Reviews* **2020**, 120  
426 (21), 11703-11809.
- 427 4. Lang, R.; Du, X.; Huang, Y.; Jiang, X.; Zhang, Q.; Guo, Y.; Liu, K.; Qiao, B.; Wang, A.; Zhang, T.,  
428 *Chemical Reviews* **2020**, 120 (21), 11986-12043.
- 429 5. Wang, A.; Li, J.; Zhang, T., *Nature Reviews Chemistry* **2018**, 2 (6), 65-81.
- 430 6. Zhang, Q.; Guan, J., *Advanced Functional Materials* **2020**, 30 (31), 2000768.
- 431 7. Qin, R.; Liu, P.; Fu, G.; Zheng, N., *Small Methods* **2018**, 2 (1), 1700286.
- 432 8. Wu, J.; Xiong, L.; Zhao, B.; Liu, M.; Huang, L., *Small Methods* **2020**, 4 (2), 1900540.
- 433 9. Hai, X.; Xi, S.; Mitchell, S.; Harrath, K.; Xu, H.; Akl, D. F.; Kong, D.; Li, J.; Li, Z.; Sun, T.; Yang, H.;  
434 Cui, Y.; Su, C.; Zhao, X.; Li, J.; Pérez-Ramírez, J.; Lu, J., *Nature Nanotechnology* **2022**, 17 (2), 174-181.
- 435 10. Zhao, S.; Chen, G.; Zhou, G.; Yin, L. C.; Veder, J. P.; Johannessen, B.; Saunders, M.; Yang, S. Z.; De  
436 Marco, R.; Liu, C., *Advanced Functional Materials* **2020**, 30 (6), 1906157.
- 437 11. Yao, Y.; Huang, Z.; Xie, P.; Wu, L.; Ma, L.; Li, T.; Pang, Z.; Jiao, M.; Liang, Z.; Gao, J.; He, Y.; Kline,  
438 D. J.; Zachariah, M. R.; Wang, C.; Lu, J.; Wu, T.; Li, T.; Wang, C.; Shahbazian-Yassar, R.; Hu, L., *Nature*  
439 *Nanotechnology* **2019**, 14 (9), 851-857.
- 440 12. Baldaguez Medina, P.; Cotty, S.; Kim, K.; Elbert, J.; Su, X., *Environmental Science: Water Research*  
441 *& Technology* **2021**, 7 (12), 2231-2240.
- 442 13. He, X.; He, Q.; Deng, Y.; Peng, M.; Chen, H.; Zhang, Y.; Yao, S.; Zhang, M.; Xiao, D.; Ma, D.; Ge, B.;  
443 Ji, H., *Nature Communications* **2019**, 10 (1), 3663.
- 444 14. Yang, H.; Shang, L.; Zhang, Q.; Shi, R.; Waterhouse, G. I. N.; Gu, L.; Zhang, T., *Nature*  
445 *Communications* **2019**, 10 (1), 4585.
- 446 15. Fonseca, J.; Lu, J., *ACS Catalysis* **2021**, 11 (12), 7018-7059.
- 447 16. Wang, C.; Gu, X.-K.; Yan, H.; Lin, Y.; Li, J.; Liu, D.; Li, W.-X.; Lu, J., *ACS Catalysis* **2017**, 7 (1), 887-  
448 891.
- 449 17. Cheng, N.; Stambula, S.; Wang, D.; Banis, M. N.; Liu, J.; Riese, A.; Xiao, B.; Li, R.; Sham, T.-K.; Liu,  
450 L.-M.; Botton, G. A.; Sun, X., *Nature Communications* **2016**, 7 (1), 13638.
- 451 18. Han, L.; Cheng, H.; Liu, W.; Li, H.; Ou, P.; Lin, R.; Wang, H.-T.; Pao, C.-W.; Head, A. R.; Wang, C.-  
452 H.; Tong, X.; Sun, C.-J.; Pong, W.-F.; Luo, J.; Zheng, J.-C.; Xin, H. L., *Nature Materials* **2022**, 21 (6), 681-  
453 688.
- 454 19. Zhou, W.; Jiang, Z.; Chen, M.; Li, Z.; Luo, X.; Guo, M.; Yang, Y.; Yu, T.; Yuan, C.; Wang, S., *Chemical*  
455 *Engineering Journal* **2022**, 428, 131210.
- 456 20. Lu, Z.; Piernavieja-Hermida, M.; Turner, C. H.; Wu, Z.; Lei, Y., *The Journal of Physical Chemistry C*  
457 **2018**, 122 (3), 1688-1698.
- 458 21. Yan, H.; Zhao, X.; Guo, N.; Lyu, Z.; Du, Y.; Xi, S.; Guo, R.; Chen, C.; Chen, Z.; Liu, W., *Nature*  
459 *communications* **2018**, 9 (1), 1-9.
- 460 22. Zhang, Z.; Feng, C.; Liu, C.; Zuo, M.; Qin, L.; Yan, X.; Xing, Y.; Li, H.; Si, R.; Zhou, S.; Zeng, J., *Nature*  
461 *Communications* **2020**, 11 (1), 1215.
- 462 23. Shi, Y.; Huang, W.-M.; Li, J.; Zhou, Y.; Li, Z.-Q.; Yin, Y.-C.; Xia, X.-H., *Nature Communications* **2020**,  
463 11 (1), 4558.
- 464 24. Liu, J.-C.; Xiao, H.; Li, J., *Journal of the American Chemical Society* **2020**, 142 (7), 3375-3383.
- 465 25. Zhou, M.; Dick, J. E.; Bard, A. J., *Journal of the American Chemical Society* **2017**, 139 (48), 17677-  
466 17682.

- 467 26. Hussein, H. E. M.; Maurer, R. J.; Amari, H.; Peters, J. J. P.; Meng, L.; Beanland, R.; Newton, M. E.;  
468 Macpherson, J. V., *ACS Nano* **2018**, 12 (7), 7388-7396.
- 469 27. Oviedo, O. A.; Reinaudi, L.; García, S. G.; Leiva, E. P. M., *Monographs in electrochemistry*.  
470 *Springer, Cham* **2016**, 1-15.
- 471 28. Szabó, S., *International Reviews in Physical Chemistry* **1991**, 10 (2), 207-248.
- 472 29. Orozco, J.; Fernández-Sánchez, C.; Jiménez-Jorquera, C., *Environmental Science & Technology*  
473 **2008**, 42 (13), 4877-4882.
- 474 30. Bewick, A.; Jovičević, J.; Thomas, B. In *Phase formation in the underpotential deposition of*  
475 *metals*, Faraday Symposia of the Chemical Society, Royal Society of Chemistry: 1977; pp 24-35.
- 476 31. Oh, H.; Park, Y.; Song, H., *The Journal of Physical Chemistry C* **2020**, 124 (37), 20398-20409.
- 477 32. Kester, J., *The Journal of Chemical Physics* **1983**, 78 (12), 7466-7472.
- 478 33. Martínez-Ruiz, A.; Palomar-Pardavé, M.; Valenzuela-Benavides, J.; Farías, M. H.; Batina, N., *The*  
479 *Journal of Physical Chemistry B* **2003**, 107 (42), 11660-11665.
- 480 34. Xu, J.; Li, R.; Xu, C.-Q.; Zeng, R.; Jiang, Z.; Mei, B.; Li, J.; Meng, D.; Chen, J., *Applied Catalysis B:*  
481 *Environmental* **2021**, 289, 120028.
- 482 35. Friedrich, J. M.; Ponce-de-León, C.; Reade, G. W.; Walsh, F. C., *Journal of Electroanalytical*  
483 *Chemistry* **2004**, 561, 203-217.
- 484 36. Ge, X.; Su, G.; Che, W.; Yang, J.; Zhou, X.; Wang, Z.; Qu, Y.; Yao, T.; Liu, W.; Wu, Y., *ACS Catalysis*  
485 **2020**, 10 (18), 10468-10475.
- 486 37. Hossain, M. D.; Liu, Z.; Zhuang, M.; Yan, X.; Xu, G. L.; Gadre, C. A.; Tyagi, A.; Abidi, I. H.; Sun, C. J.;  
487 Wong, H., *Advanced Energy Materials* **2019**, 9 (10), 1803689.
- 488 38. Saleh, M. M.; Awad, M. I.; Okajima, T.; Suga, K.; Ohsaka, T., *Electrochimica Acta* **2007**, 52 (9),  
489 3095-3104.
- 490 39. Xie, W.; Weng, L.-T.; Ng, K. M.; Chan, C. K.; Chan, C.-M., *Carbon* **2015**, 94, 740-748.
- 491 40. Feicht, P.; Siegel, R.; Thurn, H.; Neubauer, J. W.; Seuss, M.; Szabó, T.; Talyzin, A. V.; Halbig, C. E.;  
492 Eigler, S.; Kunz, D. A.; Fery, A.; Papastavrou, G.; Senker, J.; Breu, J., *Carbon* **2017**, 114, 700-705.
- 493 41. Biesinger, M. C., *Applied Surface Science* **2022**, 597, 153681.
- 494 42. Bard, A. J.; Parsons, R.; Jordan, J., *Standard Potentials in Aqueous Solution*. Taylor & Francis:  
495 1985.
- 496 43. Yi, Y.; Weinberg, G.; Prenzel, M.; Greiner, M.; Heumann, S.; Becker, S.; Schlögl, R., *Catalysis*  
497 *Today* **2017**, 295, 32-40.
- 498 44. Egorova, K. S.; Ananikov, V. P., *Angewandte Chemie International Edition* **2016**, 55 (40), 12150-  
499 12162.
- 500 45. Bard, A. J.; Faulkner, L. R.; White, H. S., *Electrochemical methods: fundamentals and*  
501 *applications*. John Wiley & Sons: 2022.
- 502 46. Zang, W.; Yang, T.; Zou, H.; Xi, S.; Zhang, H.; Liu, X.; Kou, Z.; Du, Y.; Feng, Y. P.; Shen, L.; Duan, L.;  
503 Wang, J.; Pennycook, S. J., *ACS Catalysis* **2019**, 9 (11), 10166-10173.
- 504 47. Zhao, K.; Nie, X.; Wang, H.; Chen, S.; Quan, X.; Yu, H.; Choi, W.; Zhang, G.; Kim, B.; Chen, J. G.,  
505 *Nature Communications* **2020**, 11 (1), 2455.
- 506 48. Li, Y.; Wu, Z.-S.; Lu, P.; Wang, X.; Liu, W.; Liu, Z.; Ma, J.; Ren, W.; Jiang, Z.; Bao, X., *Advanced*  
507 *Science* **2020**, 7 (5), 1903089.
- 508 49. Rudolph, J.; Jacob, C. R., *Inorganic Chemistry* **2018**, 57 (17), 10591-10607.
- 509 50. Guda, A. A.; Guda, S. A.; Martini, A.; Kravtsova, A. N.; Algasov, A.; Bugaev, A.; Kubrin, S. P.; Guda,  
510 L. V.; Šot, P.; van Bokhoven, J. A.; Copéret, C.; Soldatov, A. V., *npj Computational Materials* **2021**, 7 (1),  
511 203.
- 512 51. Gaur, A.; Shrivastava, B. D.; Srivastava, K.; Prasad, J., *X-Ray Spectrometry* **2014**, 43 (4), 238-245.
- 513 52. Fan, M.; Cui, J.; Wu, J.; Vajtai, R.; Sun, D.; Ajayan, P. M., *Small* **2020**, 16 (22), 1906782.

514 53. Kaiser, S. K.; Clark, A. H.; Cartocci, L.; Krumeich, F.; Pérez-Ramírez, J., *Small* **2021**, 17 (16),  
515 2004599.

516 54. Fu, J.; Dong, J.; Si, R.; Sun, K.; Zhang, J.; Li, M.; Yu, N.; Zhang, B.; Humphrey, M. G.; Fu, Q.; Huang,  
517 J., *ACS Catalysis* **2021**, 11 (4), 1952-1961.

518 55. Cheng, M.-J.; Clark, E. L.; Pham, H. H.; Bell, A. T.; Head-Gordon, M., *ACS Catalysis* **2016**, 6 (11),  
519 7769-7777.

520 56. Suzuta, A.; Yamazaki, K.; Gohara, K.; Uchida, T., *The Journal of Physical Chemistry C* **2022**, 126  
521 (30), 12780-12789.

522 57. Moss, A. B.; Garg, S.; Mirolo, M.; Giron Rodriguez, C. A.; Ilvonen, R.; Chorkendorff, I.; Drnec, J.;  
523 Seger, B., *Joule* **2023**, 7 (2), 350-365.

524 58. Lim, J.; Choi, S. Y.; Lee, J. W.; Lee, S. Y.; Lee, H., *Proceedings of the National Academy of Sciences*  
525 **2023**, 120 (14), e2221438120.

526 59. Overa, S.; Crandall, B. S.; Shrimant, B.; Tian, D.; Ko, B. H.; Shin, H.; Bae, C.; Jiao, F., *Nature*  
527 *Catalysis* **2022**, 5 (8), 738-745.

528 60. Huong Le, T. X.; Bechelany, M.; Cretin, M., *Carbon* **2017**, 122, 564-591.

529 61. Yang, J.; Qi, H.; Li, A.; Liu, X.; Yang, X.; Zhang, S.; Zhao, Q.; Jiang, Q.; Su, Y.; Zhang, L.; Li, J.-F.; Tian,  
530 Z.-Q.; Liu, W.; Wang, A.; Zhang, T., *Journal of the American Chemical Society* **2022**, 144 (27), 12062-  
531 12071.

532 62. Wu, Z.-Y.; Karamad, M.; Yong, X.; Huang, Q.; Cullen, D. A.; Zhu, P.; Xia, C.; Xiao, Q.; Shakouri, M.;  
533 Chen, F.-Y.; Kim, J. Y.; Xia, Y.; Heck, K.; Hu, Y.; Wong, M. S.; Li, Q.; Gates, I.; Siahrostami, S.; Wang, H.,  
534 *Nature Communications* **2021**, 12 (1), 2870.

535 63. Zhu, T.; Chen, Q.; Liao, P.; Duan, W.; Liang, S.; Yan, Z.; Feng, C., *Small* **2020**, 16 (49), 2004526.

536 64. Li, J.; Li, M.; An, N.; Zhang, S.; Song, Q.; Yang, Y.; Li, J.; Liu, X., *Proceedings of the National*  
537 *Academy of Sciences* **2022**, 119 (29), e2123450119.

538 65. Chen, G.-F.; Yuan, Y.; Jiang, H.; Ren, S.-Y.; Ding, L.-X.; Ma, L.; Wu, T.; Lu, J.; Wang, H., *Nature*  
539 *Energy* **2020**, 5 (8), 605-613.

540 66. Fan, K.; Xie, W.; Li, J.; Sun, Y.; Xu, P.; Tang, Y.; Li, Z.; Shao, M., *Nature Communications* **2022**, 13  
541 (1), 7958.

542 67. Deng, X.; Yang, Y.; Wang, L.; Fu, X. Z.; Luo, J. L., *Advanced Science* **2021**, 8 (7), 2004523.

543

544